BBA - General Subjects 1862 (2018) 2383–2392

Contents lists available at ScienceDirect

BBA - General Subjects

journal homepage: www.elsevier.com/locate/bbagen

Review

X-ray spectroscopy and imaging of selenium in living systems☆

Natalia V. Dolgova[a], Susan Nehzati[a], Sanjukta Choudhury[a], Tracy C. MacDonald[a], Nathan R. Regnier[b], Andrew M. Crawford[a], Olena Ponomarenko[a], Graham N. George[a,b,*], Ingrid J. Pickering[a,b,*]

[a] Department of Geological Sciences, University of Saskatchewan, 114 Science Place, Saskatoon, SK S7N5E2, Canada
[b] Department of Chemistry, University of Saskatchewan, 110 Science Place, Saskatoon, SK S7N0X2, Canada

ARTICLE INFO

Keywords:
Selenium
X-ray absorption spectroscopy
X-ray fluorescence imaging
EXAFS
Speciation

ABSTRACT

Background: Selenium is an essential element with a rich and varied chemistry in living organisms. It plays a variety of important roles ranging from being essential in enzymes that are critical for redox homeostasis to acting as a deterrent for herbivory in hyperaccumulating plants. Despite its importance there are many open questions, especially related to its chemistry in situ within living organisms.

Scope of review: This review discusses X-ray spectroscopy and imaging of selenium in biological samples, with an emphasis on the methods, and in particular the techniques of X-ray absorption spectroscopy (XAS) and X-ray fluorescence imaging (XFI). We discuss the experimental methods and capabilities of XAS and XFI, and review their advantages and their limitations. A perspective on future possibilities and next-generation of experiments is also provided.

Major conclusions: XAS and XFI provide powerful probes of selenium chemistry, together with unique in situ capabilities. The opportunities and capabilities of the next generation of advanced X-ray spectroscopy experiments are particularly exciting.

General significance: XAS and XFI provide versatile tools that are generally applicable to any element with a convenient X-ray absorption edge, suitable for investigating complex systems essentially without pre-treatment.

1. Introduction

Of the third-row p-block elements only selenium and bromine have confirmed roles in biological systems; selenium has the further distinction of being the element of life with the lowest crustal abundance, estimated to be around just 50 ppb [1]. Selenium is a required element for members of all six kingdoms and three domains of life, although some lineages have lost the requirement for it through evolutionary change.

In living systems the use of selenium can be divided into three broad categories: firstly as selenocysteine, the 21st amino acid, as part of essential selenoenzymes such as some glutathione peroxidases and thioredoxin reductases [2,3] or as an integral component of more complex bioinorganic systems such as the microbial Ni-Fe-Se hydrogenases [4] and some of the molybdenum and tungsten-containing formate dehydrogenases [5]; secondly as inorganic selenide as part of the active site of nicotinic acid dehydrogenases [5]; and thirdly in relatively stable organic forms such as Se-methyl-selenocysteine or L-selenocystathionine in which it is specifically accumulated by some plants called hyperaccumulators as a defense against herbivory [6–8]. Selenium is also found as L-selenomethionine, especially in plants that have no selenium-specific biochemistry (i.e. *not* the aforementioned hyperaccumulators). In such cases selenium is thought to be incorporated because of its chemical similarity with sulfur, using the same plant pathways that are used for sulfur uptake and metabolism [6,7]. L-Selenomethionine is thus often thought of as a metabolic mistake arising from its overt chemical similarity with L-methionine, although its presence in plant tissues means that it is part of many animal diets and a source of essential selenium, including for humans. Many forms of selenium are also toxic in excess [9], and for humans the differential between sufficient and toxic levels of selenium is perhaps smaller than for any other element [9].

Selenium plays essential roles in human health, especially in redox homeostasis through enzymes such as the glutathione peroxidases and the thioredoxin reductases. Acute selenium deficiency is fatal to humans and is known to cause Keshan disease [10,11] and probably also Kashin-Beck disease [12]. Keshan disease is an endemic cardiomyopathy which most often affects children between 2 and 10 years of age,

☆ This article is part of a Special Issue entitled Selenium research in biochemistry and biophysics - 200 year anniversary issue, edited by Dr. Elias Arnér and Dr. Regina Brigelius-Flohe.

* Corresponding authors at: Department of Geological Sciences, University of Saskatchewan, 114 Science Place, Saskatoon, SK S7N5E2, Canada.
E-mail addresses: g.george@usask.ca (G.N. George), ingrid.pickering@usask.ca (I.J. Pickering).

https://doi.org/10.1016/j.bbagen.2018.04.024
Received 5 March 2018; Received in revised form 24 April 2018; Accepted 27 April 2018
Available online 03 May 2018

and is named for the Keshan region of northeast China after a serious outbreak there in 1935 [11,12]. Kashin-Beck disease, which is distinct from Keshan disease and named for the researchers who first described it, is an osteoarthropathy affecting peripheral joints and spine with loss of cartilage tissues. It has also been linked to selenium deficiency, although the exact etiology is debated [13,14].

Dietary selenium is also linked to cancer in a complex manner, and with apparently conflicting results that likely relate to individual selenium status [15]. Approximately four decades ago it was shown that selenium supplements can be beneficial in cancer suppression in animals [16]. The well-known clinical study by Clark and co-workers followed, which showed a striking correlation between selenium and decreased risk of prostate cancer in men when selenium was administered in the form of selenized yeast [17]. A subsequent larger trial using L-selenomethionine supplements failed to show evidence of decreased cancer [18,19], and other work indicated an increased risk of type 2 diabetes with long-term selenium supplementation [20]. The debate about selenium status and human health is still ongoing [15,21 and refs. therein].

Both selenium deficiency and toxicity are well known in veterinary medicine [22]. Selenium deficiency is known in farm animals as a nutritional muscle dystrophy or 'white muscle disease' [22] although a range of disorders are associated with subacute selenium deficiency in veterinary medicine, including reduced fertility and increased perinatal mortality, retardation of growth and impaired immune response [22]. Although now only infrequently encountered, selenium toxicity is well known to occur in range animals such as cattle through consumption of selenium hyperaccumulating forage plants, playing a role in what is known as "alkali disease" and the "blind staggers" [23]. In humans, a chronic selenium deficiency, and distinct from the acute deficiencies such as Keshan disease, has been suggested to be a factor in the chronic low-level arsenic poisoning known as arsenicosis [24]. In this case the deficiency has been suggested to arise through regional low dietary selenium [25] combined with co-excretion of essential selenium with arsenic through formation of an arsenic-selenium excretory compound, the seleno-*bis*(S-glutathionyl)arsinum anion [24,26,27].

Because of these considerations, the chemistry of selenium in living organisms is of considerable interest. This review will discuss in situ methods for visualization of selenium associated with X-ray spectroscopy. These powerful and emerging tools can provide molecular-level information on samples under a variety of conditions, often requiring little or no pretreatment. The methods to be discussed include both X-ray absorption spectroscopy and X-ray fluorescence imaging, with examples taken from recent applications of the methods. These methods depend heavily upon synchrotron radiation which is only available at specialized locations. The primary focus of this review is the methods themselves, and while examples will be used, we do not intend to give a comprehensive review of applications. A perspective on future methods, using advanced X-ray spectroscopy, with an overview of a potential next-generation of experiments will also be provided.

2. Physical background: absorption of X-rays through core electron excitation

X-ray absorption is elementally specific and is due to excitation of a core electron of a particular atom. For selenium the K-edge absorption corresponds to excitation of the most tightly bound 1s electrons, and occurs at energies close to 12,658 eV. The absorption of a photon through 1s photoexcitation creates a 1s core-hole which is then rapidly filled by decay of higher bound electrons with concomitant release of an X-ray fluorescent photon, or alternatively with emission of an Auger electron. Fig. 1 shows a schematic diagram of the physics of X-ray absorption. The timescale of the photoexcitation event is extremely rapid, in the vicinity of 20 zeptoseconds for Se K-edge excitation, while the lifetime of the 1s core-hole will be close to ¼ femtoseconds. The major X-ray fluorescence emission lines follow simple dipole selection rules,

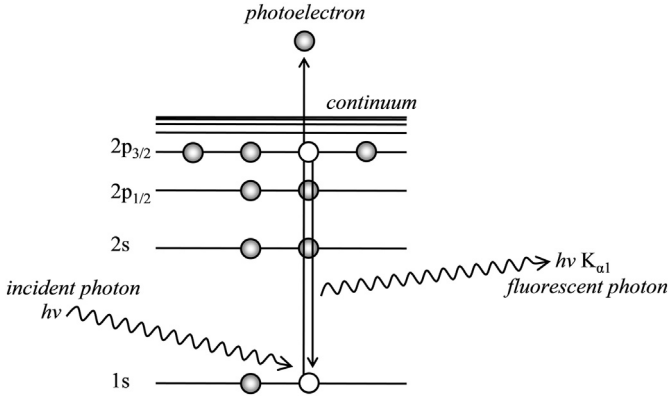

Fig. 1. Schematic diagram illustrating the physics of X-ray absorption spectroscopy. The incident X-ray photon is absorbed by the core 1s electron which is excited into the continuum as a photoelectron with the formation of a 1s core hole. This core hole is rapidly filled by decay of a higher electron ($2p_{3/2}$) with the concomitant emission of an X-ray fluorescent ($K_{\alpha 1}$) photon and creation of $2p_{3/2}$ core hole.

so that the most intense fluorescence lines correspond to transitions with $\Delta l = \pm 1$. Thus, the $K_{\alpha 1}$ and $K_{\alpha 2}$ fluorescence emission lines arise from $2p^3/_2 \rightarrow 1s$ and $2p^1/_2 \rightarrow 1s$ transitions, respectively, and the $K_{\beta 1}$ and $K_{\beta 3}$ from $3p^3/_2 \rightarrow 1s$ and $3p^1/_2 \rightarrow 1s$ transitions, respectively.

3. Selenium X-ray absorption spectroscopy

An X-ray absorption spectroscopy (XAS) experiment typically monitors the absorption of a monochromatic beam of X-rays (either directly or indirectly) as a function of the incident energy. XAS can be used to provide information on metal or metalloid containing specimens. XAS requires no pre-treatment or extraction, and thus provides a tool that can probe chemical species in situ. Essentially any type of sample relevant to biological systems can be examined, which can include purified biomolecules, cell cultures, tissues, intact small organs or organisms, as well as environments or contaminants such as soil, sediment, dust or water. The absorption edge is a sudden rise in the X-ray absorption coefficient which occurs when there is sufficient X-ray energy to excite a core electron. Since this is an atomic-level effect, XAS is element-specific, with the absorption edge within a narrow energy range corresponding uniquely to one element; for example, Se XAS can never be confused with S XAS since, though chemically similar, these elements differ greatly in atomic number. The spectrum can be divided into two overlapping regions of arbitrary extent – the near-edge spectrum which is a structured spectral region within approximately 50 eV of the absorption edge, and the extended X-ray absorption fine structure (EXAFS), which comprises oscillations on the high-energy side of the absorption edge, and which can be accurately interpreted in terms of a local radial structure [5]. Fig. 2 shows a typical selenium K-edge X-ray absorption spectrum, with the near-edge and EXAFS regions, together with the X-ray emission spectrum of a more dilute solution (approaching that of biological samples) measured with a solid-state energy dispersive detector (a high-purity Ge 30-element array).

We have previously noted that the nomenclature of near-edge spectra is very confused [5], with many acronyms used to describe the same spectroscopic region, and sometimes the same acronym used to describe different spectroscopic regions. The near-edge region is often also referred to as the X-ray absorption near-edge fine structure or XANES. The observed structure within the near-edge region is due to transitions from the core level (1s for a K-edge) to unoccupied molecular orbitals of the system. Thus, with K-edges and 1s excitation intense $\Delta l = \pm 1$ dipole-allowed transitions are observed in near-edge spectra. Because selenium chemistry predominantly involves the 4p levels, the spectra show intense $1s \rightarrow 4p$ transitions and are exquisitely

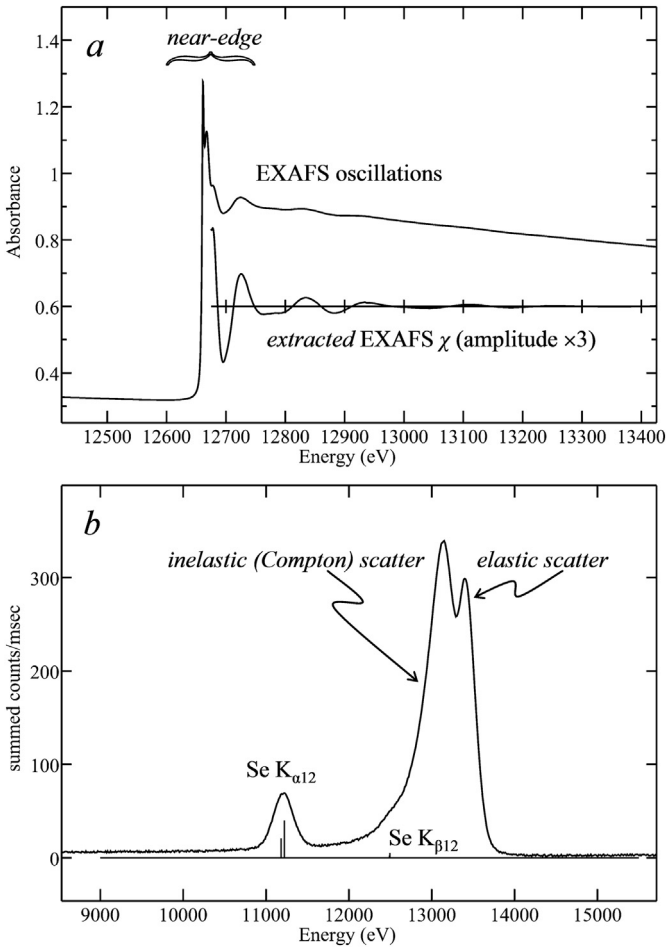

Fig. 2. Examples of selenium K-edge X-ray absorption and X-ray emission spectra. *a* shows the spectrum measured in transmittance of a 0.1 M solution of selenophene C_4H_4Se in toluene. The near-edge region is indicated, together with the EXAFS vertically expanded by a factor of 3 in the inset. *b* shows the X-ray emission spectrum of a 5 mM aqueous solution of selenate $[SeO_4]^{2-}$ in the presence of 25% v.v. glycerol pH 7.5 recorded with a Ge detector 30-element array. The energies of the characteristic selenium fluorescence are shown by the stick diagram in *b*.

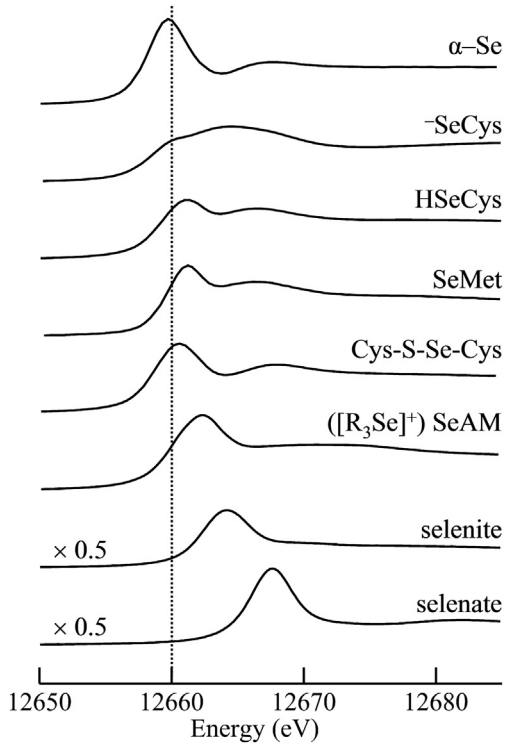

Fig. 3. Selected selenium K-edge X-ray absorption near-edge spectra of biologically relevant standard compounds. The α–Se is a colloidal (nanoparticulate) sample, all other compounds are ca. 1 mM in buffered aqueous solution at pH 7.4 in the presence of 25% v/v glycerol to prevent ice diffraction artifacts. The vertical scale of the bottom two traces has been reduced by a factor of two, and the vertical line at 12660 eV is included to guide the eye to subtle shifts between similar spectra.

sensitive to speciation as they probe those levels that are directly involved in the chemistry of selenium. The spectra are a sensitive indicator of electronic structure, and can be regarded as giving a "fingerprint" for chemical speciation. Although this is an obvious limitation, we note that true molecular-level speciation is not provided by XAS. The spectra are sensitive to the electronic structure, so that while local structure is very important long-range structure can often matter only subtly. For example, while the XAS spectrum of L-selenocysteineate is quite distinct from that of L-selenomethionine [28], L-selenomethionine in solution appears very similar to L-selenomethionine in a protein, and also similar to Se-methyl-L-selenocysteine and dimethylselenide [28], as all are aliphatic selenides with the same local selenium environment or selenium "functional group", to wit, $-CH_2-Se-CH_2-$.

Fig. 3 shows the near-edge spectra of a series of different biologically relevant selenium compounds. Such spectra of known standards are sometimes referred to as model compound spectra. One advantage of the near-edge region of the spectrum is that it can be quickly collected with adequate signal to noise, and we have previously shown using conventional XAS experiments that near-edge spectra of samples approaching 1 μM are possible [29,30]. The spectra are quantitative, as the edge jump is proportional to the amount of selenium present. Mixtures of more than one selenium type can be analyzed by least-squares fitting of linear combinations of spectra of known standards (e.g. Fig. 3) to the spectrum of an unknown selenium species, such as the selenium present in a biological tissue. Such "speciation" analyses can only determine selenium chemical type rather than individual molecules, as described above, and rely on having authentic and biochemically relevant selenium standards available for spectrum measurement. However, the ability to measure such mixtures in situ in biological tissues with very little sample preparation, has made near-edge XAS analysis a highly valuable technique.

In contrast to the near-edge, EXAFS is more difficult to collect with good signal to noise, and may not always be practical for dilute samples. Some early applications of EXAFS suffered from over-interpretation of the data, but when used with appropriate caution EXAFS is very well suited to the study of biomolecules [5,31,32]. We now consider the physical basis for the EXAFS in simplified terms; for a more complete description the reader is referred elsewhere [33]. EXAFS can be qualitatively understood by considering the photoelectron resulting from core electron photo-excitation as a de Broglie wave that will be back-scattered by nearby atoms; the back-scattered wave will differ in phase relative to the outgoing and interference will result, with the absorption being at maximum and a minimum for constructive (in phase) and destructive (out of phase) interference, respectively. As the X-ray energy is experimentally increased above the absorption threshold, the energy of the photo-electron increases and hence the de Broglie wavelength decreases, causing successive periods of constructive and destructive interference and an oscillatory modulation of the X-ray absorption; this is the EXAFS. The EXAFS frequency is sensitive to the absorber-backscatterer distance, to a first approximation the amplitude is directly related to the size (atomic number) of the backscatterer, and in practice both phase and amplitude are sensitive to the identity of the backscatterer. The EXAFS is typically shown as a function of the photo-

electron wave vector k, which is related to the X-ray energy E by $k = \sqrt{(E - E_0)2m_e/\hbar^2}$ where E_0 is the photo-ionization threshold energy, m_e is the electron rest mass and $\hbar$ is Plank's constant divided by 2π. The EXAFS χ is defined as the oscillatory part of the absorption coefficient μ where the unstructured absorption is μ_0 so that $\mu = \mu_0(1 + \chi)$; χ is thus dimensionless but is typically plotted with k^3-weighting to counteract various losses in amplitude that occur with increased k. Experimental EXAFS is the combined backscattering from all the nearby atoms, and in some cases this can give rise to quite complicated spectra.

The data is analyzed by fitting a theoretical model to the experimental data; since theoretical models are very well advanced such analysis can give very accurate estimates of interatomic distances R, usually ± 0.02 Å, with less accurate coordination numbers N and neighbor identities, usually within 20%. EXAFS has inherent limitations; firstly as with many model-building analytical approaches, an incorrect model can potentially yield incorrect conclusions, moreover geometric information is usually lacking so only radial structure information is available. In addition, given an appropriate arrangement of backscatterers the EXAFS oscillations from different backscatterers can also cancel, although usually only partially [e.g. 31,34–35], so that absence of observed backscattering does not mean that a neighbor atom is absent, for example with yeast copper metallothionein no Cu···Cu EXAFS is observed, despite the presence of a well-defined cluster due to such cancellation [34]. As an example of the analytic method we will consider a simple standard compound, the aromatic molecule selenophene, C_4H_4Se in which selenium contributes two electrons to the Hückel aromatic sextet, the raw XAS data for which is shown in Fig. 2a. Fig. 4 shows the EXAFS oscillations for a solution of selenophene plus the EXAFS Fourier transform, together with the curve-fitting analysis in which the EXAFS oscillations are fitted to an experimental model using a theoretical description. Another important limitation of EXAFS is that it has poor bond-length resolution. The EXAFS resolution can be simply defined as the ability to discriminate two different absorber-backscatterer distances from atoms of the same type. The EXAFS resolution is directly related to the extent of the data in k-space and is approximately given by $\Delta R \approx \pi/2k$. For example, if two different S–C distances were to differ by less than 0.1 Å then the data of Fig. 4 would not allow independent determination of these, but instead this difference would manifest as an apparent increase in the disorder. Thus, while EXAFS has excellent accuracy in the determination of mean interatomic distances, the resolution can often be poor. We have explored the simple, but experimentally challenging expedient of extending the k-range of the data to help overcome this limitation [36]. Experimental arrangements for XAS have recently been described in detail [37], and we will therefore review them only briefly here. Experimentally, XAS is usually measured by monitoring the characteristic X-ray fluorescence, which for selenium would normally be the combined $K_{\alpha 1}$ and $K_{\alpha 2}$, most commonly using solid-state energy dispersive detectors or arrays thereof [38,39]. Such detectors are often count-rate limited, so that with modern beamlines filters and Soller slits [38] must be used to keep the detector response within a pseudo-linear regime [39]. Fig. 5 shows a schematic of an experimental XAS setup, with a sample maintained at low temperature in a cryostat in order to minimize photo-damage, to preserve the biological sample and to maximize the EXAFS signal due to minimization of thermal vibrations.

4. Selenium X-ray fluorescence imaging

The development of beamlines employing micro or nano-focused X-ray beams enables imaging techniques that collectively are known as X-ray fluorescence imaging (XFI) [39]. A variety of other acronyms are used for the same method, including SRIXE (synchrotron radiation induced X-ray emission), μ-XRF (micro X-ray fluorescence), XFM (X-ray fluorescence microscopy), XFM (X-ray fluorescence mapping) and others [39]. Since there is no standard, here we will use the acronym XFI. The mechanisms of production of micro-focused X-ray beams have recently been reviewed, and rather than reiterating the details here we refer the reader to prior discussion [39, and refs. therein]. In an XFI experiment, a small beam is used to interrogate different regions of the sample, with the X-ray fluorescence being monitored using an energy dispersive detector, and the sample being moved systematically so that an image is built up.

Raw XFI data is an X-ray emission spectrum, with contributions from both sample and background (e.g., elastic and inelastic scattering, impurities in the sample holder, secondary hutch fluorescence, and any detector dark current). A number of alternative software packages exist for the processing of XFI data [40–47]. When processing XFI data, the simplest analytical approach is to sum all the counts in an energy region of interest corresponding to a particular elemental emission and to attempt per-pixel quantification by comparison with known standards. For data visualization during experiments, this is the most common approach. However, due to the inherently poor energy resolution associated with energy dispersive detectors, such summing is obviously approximate and quantitative analysis with fitting of the emission spectrum is superior [48]. For fitting, XFI spectra are typically fit as a sum of a background function together with one or more fluorescence peaks, often modelled as modified Gaussians [49,50]. The most

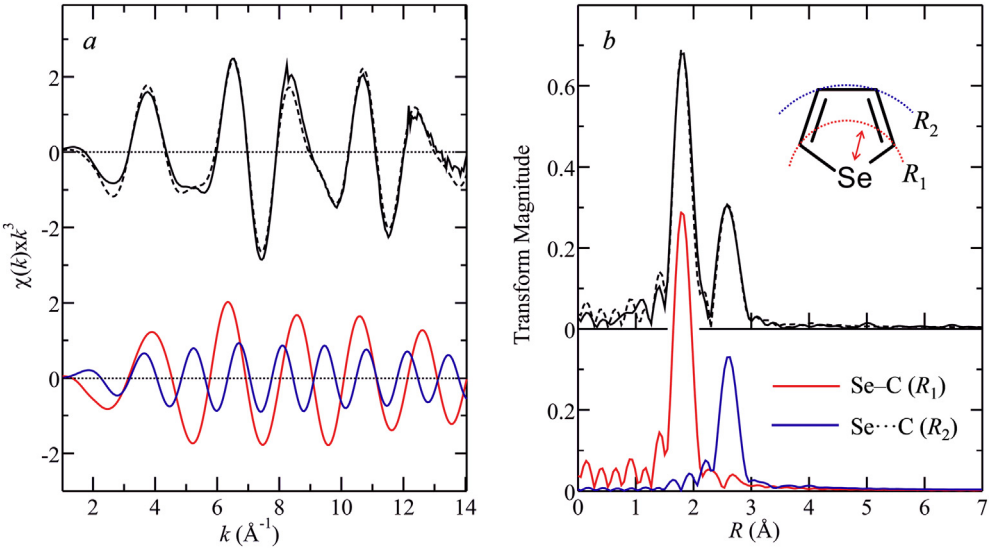

Fig. 4. EXAFS data analysis for selenophene. *a* illustrates the EXAFS, showing both experimental (——) and theoretically modelled (- - - - -) EXAFS oscillations. The theoretical EXAFS is fitted to the experimental data by non-linear optimization of structural parameters such as interatomic distances. The lower traces show the EXAFS from individual first shell (——) and second shell (——) Se–C EXAFS which are combined to make the theoretically modelled data. *b* shows the corresponding EXAFS Fourier transforms of the curves in *a*, together with the structure of selenophene. The EXAFS curve-fitting gives Se–C interatomic distances of 1.86 and 2.69 Å for first shell (R_1) and second shell (R_2), respectively.

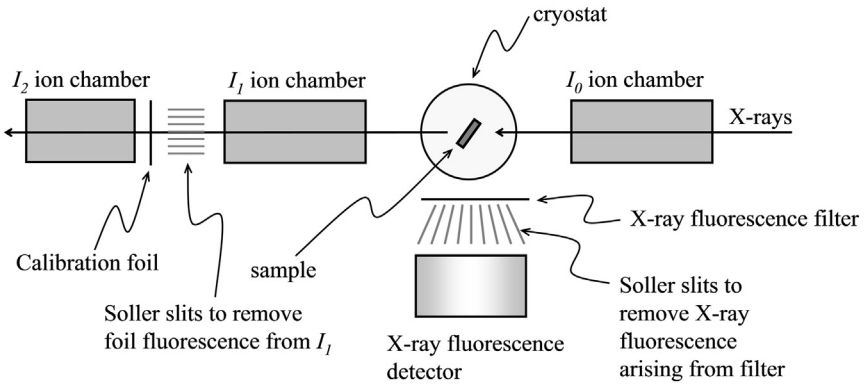

Fig. 5. Plan view schematic diagram of the experimental apparatus for X-ray absorption spectroscopy. The monochromatic X-ray beam from a synchrotron radiation source enters through the right side of the figure, and its intensity registered by the ion chamber detector I_0. The beam continues through the sample located inside a cryostat and proceeds through the ion chamber I_1, through a reference foil which is used for X-ray energy calibration, and then through a third ion chamber I_2. The absorbance of the sample is $\ln(I_0/I_1)$ and that of the reference foil is $\ln(I_1/I_2)$. X-ray fluorescence is measured by the fluorescence detector located at 90° to the incident beam to minimize X-ray scatter, and the absorbance is proportional to (F/I_0), where F is the fluorescence signal. The fluorescence filter is used to preferentially absorb scattered X-rays and transmit fluorescence; for Se K-edge XAS an arsenic filter would be used as the As K-edge is above the selenium Kα energy and below the scatter energy.

common approach to accounting for a background is to initially remove baseline [45,50–53], in many cases, on a per-pixel basis. However, it has recently been suggested that per pixel baselines can result in significant, systematic errors in quantitation [48]. Alternatively, one can usually take advantage of the fact that most XFI data contain some non-sample regions; and thus those regions can be used to define a background in the form of a blank. Regardless of the specifics of fitting, once XFI data is fitted, each pixel's fluorescence counts are converted to elemental mass per area (e.g., μg/cm^2) [39] via simple comparison to the counts from a known standard collected under identical conditions.

Fig. 6 shows a schematic of an XFI experiment, together with an example of experimental data for a whole intact larval stage zebrafish exposed to low levels of Hg^{2+} in water. In many XFI experiments sections of samples are examined, but intact small organisms (e.g. Fig. 6) or intact tissue fragments (e.g. leaves) may also be investigated directly. We note here that biological samples have an inherent variability that makes collection of replicate data important. This must be balanced by the time taken to collect adequate data and with necessarily limited synchrotron radiation access, and typically between three and five such replicates are collected. While XFI alone provides maps of elemental

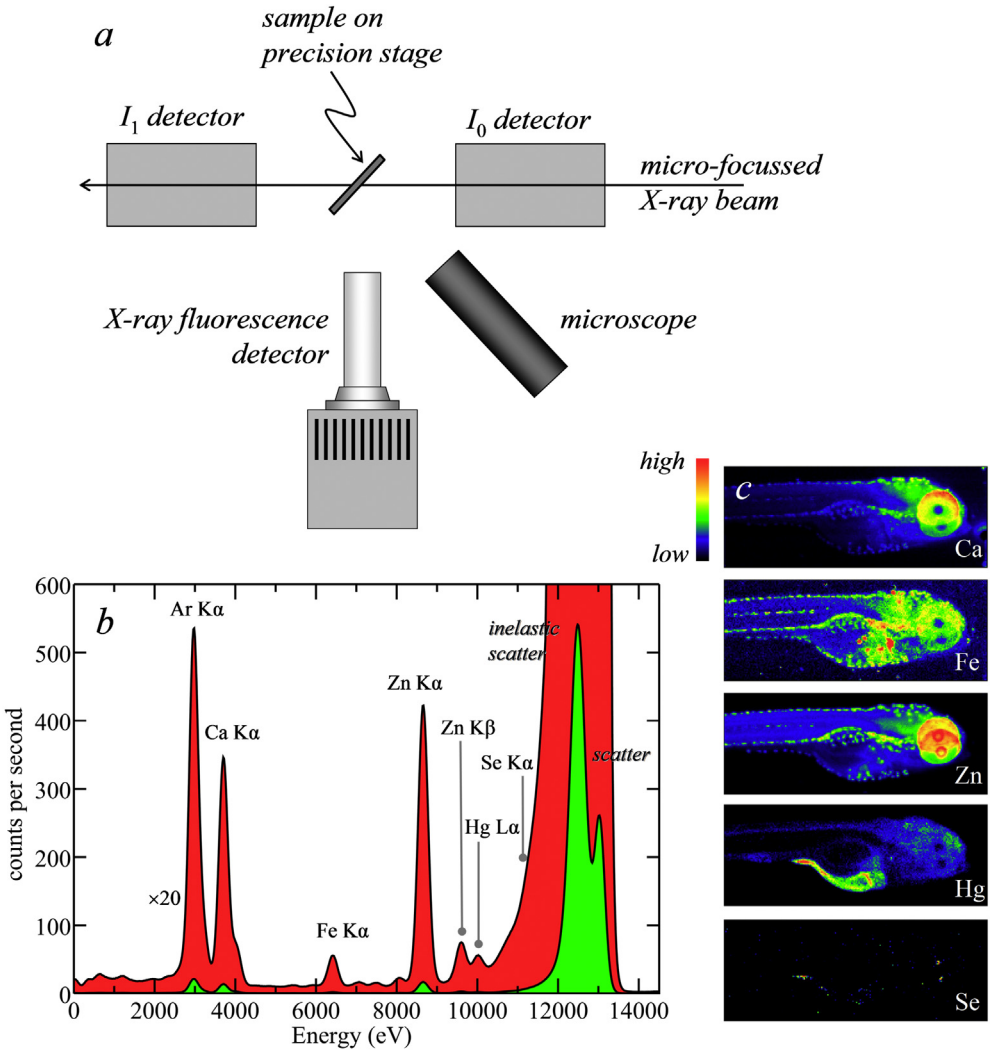

Fig. 6. X-ray fluorescence imaging. *a* shows a schematic of the experimental setup (plan view), and *b* shows a typical X-ray fluorescence detector output showing fluorescence from elements within the sample plus atmospheric argon, with a dominant contribution from the X-ray scattering. The green-filled curve shows the whole spectrum, including the intense scatter peak, while the red-filled curve has been expanded vertically by ×20 to allow the fluorescence to be seen more clearly. *c* shows the images of the different elements of the sample obtained by fitting the fluorescence peaks in *b*; in this case a four-day post-fertilization larval stage zebrafish which had been exposed to 0.2 μM $HgCl_2$.

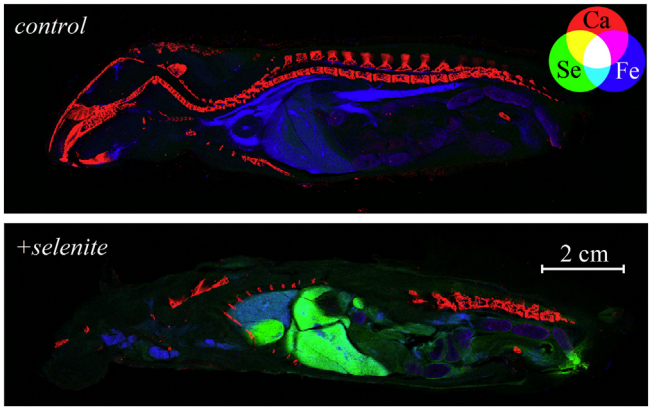

Fig. 7. Example of large-format X-ray fluorescence imaging. The figure shows longitudinal lyophilized cryosections of Chinese hamster as tri-color plots in which calcium is shown in red, selenium in green and iron in blue. The sections compared are of an untreated hamster (*control*) and of a hamster intravenously injected with a solution of sodium selenite at 2.52 mg kg^{-1} (+*selenite*) and euthanized 30 min later (all operations were carried out under anesthetic).

distribution for all elements that have absorption edges below the incident X-ray energy, micro X-ray absorption spectroscopy (μ-XAS) can provide speciation on image pixels of interest by simply moving the sample to a location and recording an XAS spectrum. With suitable experimental equipment, quite large samples may be examined by XFI, and Fig. 7 shows an example of modest size, longitudinal cryosections of Chinese hamster, with and without selenium; at the largest, XFI of samples approaching a meter across have been reported.

A special category of XFI experiments is chemically selective XFI. Here incident excitation energies are used, and these have been carefully selected to preferentially excite specific chemical species in the sample. Selenium was the first element to be investigated by chemically specific XFI [54]. These experiments were conducted at the spatial resolution of 100 μm, comparatively poor resolution relative to modern applications, but represented the first demonstration of this technology. The selenium chemical forms in the hyperaccumulator *Astragalus bisulcatus*, which accumulates high levels of Se-methyl-L-selenocysteine in its tissues, were shown to be predominantly reduced organic selenides in young leaves but in older leaves were present predominantly as selenate [54]. Subsequent work at higher resolutions (ca. 5 μm) demonstrated that selenium was in the tissues, centrally localized in cells, presumably in the cellular vacuole, and that only low levels were present in the leaf hairs or trichomes [55].

Selenium XFI has since been used to examine samples ranging from bacterial biofilms [56] to vertebrate tissues [57], an example of which is given in Fig. 8, which shows comparison of selenium distribution and accumulation level in sections of larval stage zebrafish at six days post-fertilization, treated with either selenite or L-selenomethionine. The difference in selenium uptake and distribution is strikingly different between the two different chemical forms. Treatment with L-selenomethionine results in elevated selenium concentrations throughout the body and very high concentrations in melanin-containing cells, of up to 200-fold higher than other tissues [57]. When selenite is administered selenium accumulates throughout the whole body without accumulation in the pigment cells [57]. Although studies to date have not addressed this, we note that these types of experiment could also be used to track selenium metabolism and changes in distribution over time by collecting samples from different time points after exposure to different compounds. Selenium K-edge XFI has also been used to examine selenium in mammalian tissues [27]; of particular note are a series of publications that describe the importance and unanticipated roles of selenium in the follicle maturation in ovaries [58,59], and in kidneys, showing that selenium is concentrated in the basement membrane of proximal tubules [60]. XFI of selenium and arsenic have also been used

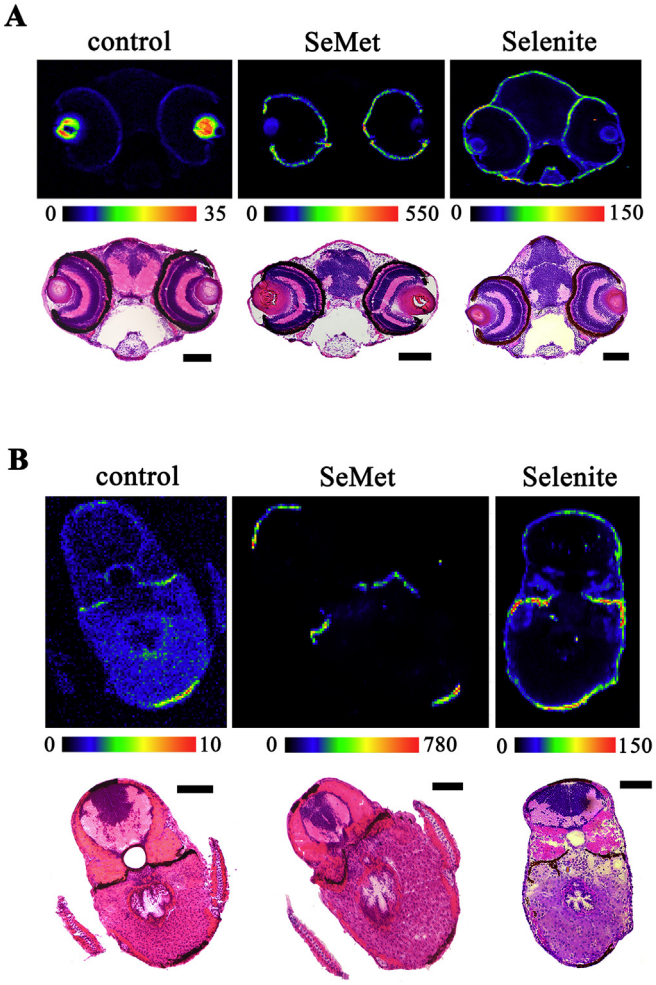

Fig. 8. X-ray fluorescence imaging of cryosections of larval stage zebrafish (6 days post-fertilization) following exposure to low levels of L-selenomethionine or selenite. **A** shows eye sections and **B** trunk sections. In both **A** and **B** the upper panels show the XFI data and the lower panels the conventional histology carried out on adjacent section to that used for XFI. The color gradient bar shows areal densities (ng/cm^2), each image is a representative of three or more samples with repeats showing very similar distributions and range if areal densities. Striking differences in uptake and distribution of selenium with the different chemical forms are obvious.

to examine co-location of these elements in various tissues of hamster, using lyophilized whole-body sections [27].

Although this review is restricted to X-ray based methods, we note that combining XFI with other imaging techniques can provide much deeper insights than are available with any one method, and such multi-modal approaches have recently been exploited [61]. A recent review has discussed other methods in some detail [39], and we therefore only will touch briefly on this here. Examples of complementary methods include imaging methods exploiting vibrational spectroscopy such as Fourier transform infrared (FTIR) or Raman imaging [61] which give molecular-level information on tissue and metabolite composition, together with conventional methods such as histological staining, and immunohistochemistry. Positron emission tomography or single-photon emission computed tomography [e.g. 62] can give pulse-chase type information that is highly complementary to that from XFI, although for selenium the PET-capable isotope ^{73}Se has a half-life of only 7.1 h, so its use may be restricted to the vicinity of facilities for its manufacture. Mass spectrometry imaging (MSI) methods deserve special mention because they can provide both very similar information to XFI and highly complementary information.

Thus, laser-ablation inductively-coupled-plasma mass-spectrometry (LA-ICP-MS) provides similar elemental mapping information to XFI, and while both resolution and sensitivity can be more limited LA-ICP-MS has the enormous advantage of not requiring a synchrotron radiation source. Matrix-assisted laser desorption ionization (MALDI) mass spectrometry can resolve a range of bio-molecules, and both methods provide highly complementary information to XFI [39]. Correct spatial registration of the sample for application of different methods is important, and the order of data acquisition is also important, for example FTIR is less destructive than XFI and ideally should be measured first.

5. Three dimensional methods

5.1. Confocal X-ray fluorescence imaging

Confocal X-ray fluorescence imaging [39] is a variant of conventional XFI that enables three dimensionally resolved imaging of samples by employing an additional focusing optic in front of a solid-state energy dispersive X-ray fluorescence detector. The experiment is aligned so that the foci of the incident X-ray beam and the detector focusing optic coincide, defining a probe volume. To collect a confocal image the sample is moved so that the probe volume interrogates a plane of interest within a sample [39]. The detector focusing optic can be a polycapillary [63] although recent work using Collimating Channel Arrays [64–66] shows that these devices can offer superior spatial resolution for the confocal plane. The ability to collect three dimensionally resolved images allows imaging of a region of interest within an intact larger specimen, a key advantage to the application of the confocal approach. In contrast, conventional XFI requires a physical thin section of the sample, which is problematic in cases where the sample cannot be sectioned such as unique cultural heritage samples [67,68], fragile archaeological samples [69] and some biological samples [70], especially if these may be prone to contamination [71]. Another important advantage of confocal mode is that the probe volume can also be used directly for confocal μ–XAS [67,72] which enables determination of the localized chemical speciation of elements. Additionally, confocal XFI can show higher signal to noise ratio because of superior background rejection, since the detector collects fluorescence only from the probe volume and rejects both fluorescence and scattered radiation from off-focus regions of the sample and the experimental environment, which may include the substrate upon which the thinned sample is mounted.

Fig. 9 shows an example of experimental confocal XFI showing the distribution of selenium and zinc in an intact larval stage zebrafish (72 h post-fertilization) which had received high maternally-transferred selenium [70]. The figure shows three confocally generated sections within the sample, each positioned 60 μm deeper into the sample relative to the top. The top and middle sections respectively show the right and left eye-lens with a substantial selenium accumulation. While this preferential accumulation is likely through the incorporation of selenium into L-methionine-containing crystallin proteins of the lens, it is expected to be related to larval life stage because of rapid early lens development in order for the establishment of vision for survival [70].

Disadvantages of confocal XFI include exposure of the sample to a high radiation dose, especially if collection of serial confocal images is performed for 3-dimensional reconstruction, which usually necessitates the use of cryogenic sample cooling. Moreover, elements of low atomic number can be difficult to observe in such confocal experiments, relative to measurements using physical sample sections, because the X-ray fluorescence from light elements will not penetrate adequately through the thicker sample [26].

5.2. X-ray fluorescence tomography

X-ray fluorescence tomography [39] is another method for three-dimensional imaging of unsectioned samples, which is increasingly being applied to questions in the life and environmental sciences. In this experiment, a sample is translated through a dimension x as a function of a rotation angle φ with axis normal to x so that the spatially fixed micro-focused X-ray beam produces an X-ray fluorescence sinogram (a plot of fluorescence intensity in the φ–x plane) which is subjected to tomographic reconstruction to produce a cross-sectional slice of the object [39]. The sample can then be vertically translated to collect another sinogram and hence another cross-sectional slice and finally, a three dimensional image is constructed from the assembled tomographic slices. While confocal XFI and X-ray fluorescence tomography both allow study of the three-dimensional elemental distributions within intact samples, X-ray fluorescence tomography requires the sample to be rotated through a substantial angle, which limits the morphology of the sample. In addition, confocal XFI may be favored when the measurement of chemical forms of elements using μ–XAS is of interest because the confocal measurement can be used to interrogate an individual voxel (volume element) and the μ–XAS simply recorded. In contrast, with tomography voxel-specific data is only available from tomographic reconstruction and μ–XAS spectra would require collection of substantially more data. Similarly to confocal XFI, X-ray

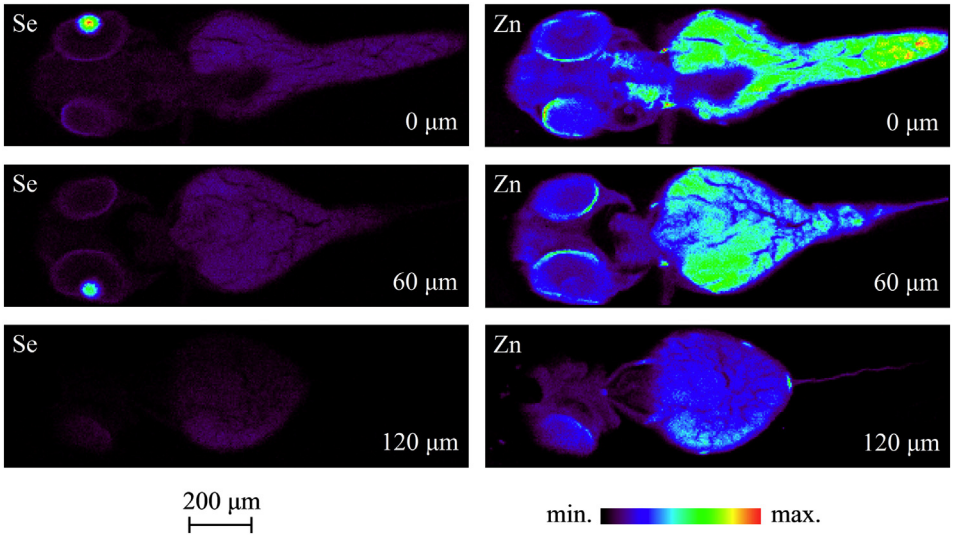

Fig. 9. Confocal X-ray fluorescence imaging showing the distribution of Se and Zn in a fixed but un-sectioned larval stage zebrafish. Sequential confocal slices are shown, each displaced relatively by 60 μm.

fluorescence tomography may show artifacts and limited access to the low atomic number elements due to attenuation of the incident and fluorescent X-rays, and the possibility of radiation damage is also a concern.

6. Advanced spectroscopy for future applications

The advent of so-called advanced spectroscopy using high resolution crystal optics affords new opportunities that have the potential to revolutionize the field. Here we give only a brief overview; for more details the reader is referred to more specialized publications [73]. These advanced spectroscopy methods require small and very intense monochromatic X-ray beams plus crystal optics that are capable of measuring X-ray fluorescence with considerably better resolution than the natural linewidth [74]. The primary method of interest for application to biological samples is high energy resolution fluorescence detection (HERFD) XAS, which seeks to overcome the lifetime broadening arising from the short lifetime of the core hole generated by the primary photoexcitation event. Heisenberg's uncertainty principle can be stated as $\Delta t \Delta E \geq \hbar^2/2$ where Δt and ΔE are the core-hole lifetime and the spectroscopic lifetime broadening, respectively. Thus, very short core-hole lifetimes will give rise to broad spectra, which is a major limitation of XAS. Fig. 10 gives a schematic overview of the physics behind the HERFD method; when the fluorescence is detected with sufficiently high resolution then the observed spectroscopic broadening is no longer controlled by the lifetime of the core-hole generated by the primary photo-excitation, but instead by the lifetime of the core-hole generated by the decay of the electron to give the fluorescent photon and fill the core-hole. This gives exquisitely sharp spectra, with consequently increased speciation sensitivity. To date these methods have been little used in the life sciences, but their potential is substantial. An obvious extension of HERFD is HERFD-XFI, and μ-HERFD-XAS where the chemically specific XFI or μ-XAS described above is performed using the specialized HERFD experimental apparatus. As with other methods that depend upon high intensity X-ray beams, HERFD-XAS is susceptible to problems from photo-damage of samples. Typically experiments use cryogenic temperatures to help protect the sample, and if signal averaging is used then the sample may be translated so that the beam interrogates a fresh spot with every scan. One major pitfall of the HERFD method is that crystal analyzers are usually element-specific. This is because in order to get the exceptional analyzer energy resolution of ~0.8 eV that is required to observe a bona fide HERFD effect, the Bragg angle must be as close as possible to 90°. Thus, to measure Se $K_{\alpha 1}$ HERFD, with fluorescence centered upon an energy of about 11,224 eV, a Si(844) spherical analyzer crystal with a Bragg angle θ_B of about 85.2° is used. Other analyzers, such as Ge(844), have θ_B ~73.1° which will be too far from the ideal of 90° to observe a true HERFD spectrum having substantially enhanced spectroscopic energy resolution. Moreover, the beam size on the sample must also be as small as possible, or likewise the energy resolution will degrade.

7. Conclusions

Despite the fact that selenium is the rarest of the essential elements both its roles and importance in living organisms are now well established. Notwithstanding this progress, there remain a number of outstanding and important questions or uncertainties related to selenium biochemistry. Examples relevant to human health include selenium's roles as a cancer preventative agent, in type 2 diabetes, and in the arsenicosis epidemic in Bangladesh. The X-ray based methods described in this review provide a direct and versatile means of investigating selenium in situ in organisms, tissues and in purified protein systems. The methods that we have discussed are useful in a wide variety of samples conditions, and require very little or no sample pre-treatment, which is important when studying delicate biological samples. While the continuous improvement of X-ray sources, detectors and associated electronics will enable improved sensitivity, and energy and spatial resolutions of these techniques, the implementation of new

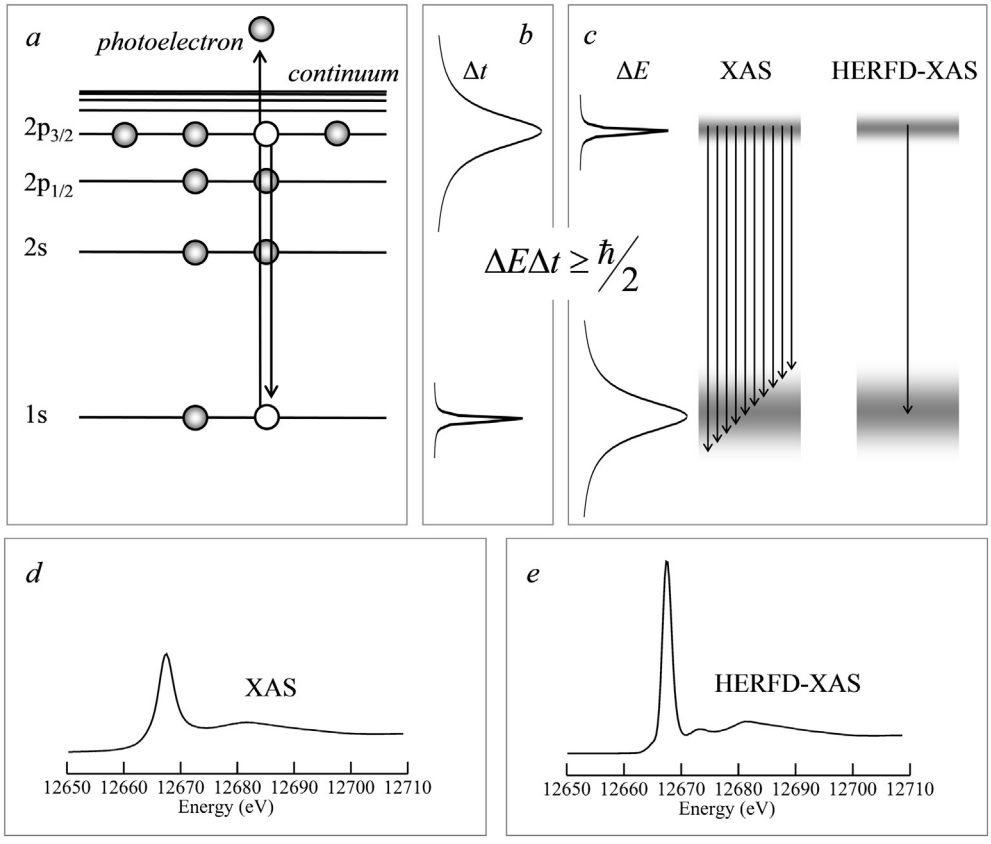

Fig. 10. Schematic of the physical basis for high energy resolution fluorescence detection (HERFD) XAS. *a* shows a schematic of the photoexcitation and fluorescence emission, *b* shows the core-hole lifetimes, *c* the lifetime broadening together with the transitions for XAS and HERFD-XAS recorded by monitoring the X-ray fluorescence, *d* and *e* respectively show the XAS and HERFD-XAS for a dilute aqueous solution of selenate $[SeO_4]^{2-}$.

experimental approaches combining various conventional, imaging and spectroscopic modalities will allow more comprehensive research on selenium. Particularly, the application of HERFD XAS and its possible extension to chemically selective XFI have opened up new opportunities for selenium research.

Transparency document

The Transparency document associated with this article can be found, in online version.

Acknowledgements

Work at the University of Saskatchewan was supported by the Natural Sciences and Engineering Research Council of Canada (RGPIN 04632-2014 to G. N. G. and RGPIN 05810-2016 to I. J. P.), the Saskatchewan Health Research Foundation (G.N.G., I.J.P.), the Canada Foundation for Innovation (to I.J.P.), the Government of Saskatchewan (I.J.P.) and Canada Research Chair awards (G.N.G. and I.J.P.). S.N. acknowledges the Dr. Rui Feng Scholarship. Portions of this research used the Stanford Synchrotron Radiation Lightsource, SLAC National Accelerator Laboratory, use of which is supported by the U.S. Department of Energy, Office of Science, Office of Basic Energy Sciences under Contract No. DE-AC02-76SF00515. The SSRL Structural Molecular Biology Program is supported by the DOE Office of Biological and Environmental Research, and by the National Institutes of Health, National Institute of General Medical Sciences (including P41GM103393). The contents of this publication are solely the responsibility of the authors and do not necessarily represent the official views of NIGMS or NIH.

Portions of this research also used resources of the Advanced Photon Source, an Office of Science User Facility operated for the U.S. Department of Energy (DOE) Office of Science by Argonne National Laboratory, and was supported by the U.S. DOE under Contract No. DE-AC02-06CH11357, and the Canadian Light Source and its funding partners.

References

[1] K.H. Wedepohl, The composition of the continental crust, Geochim. Cosmochim. Acta 59 (1995) 1217–1232.
[2] P. Dammeyer, E.S.J. Arner, Human protein atlas of redox systems – what can be learnt? Biochim. Biophys. Acta 1810 (2011) 111–138.
[3] M. Dagnell, E.E. Schmidt, E.S.J. Arner, The A to Z of modulated cell patterning by mammalian thioredoxin reductases, Free Radic. Biol. Med. 115 (2018) 484–496.
[4] C.S.A. Baltazar, M.C. Marques, C.M. Soares, A.M. DeLacey, I.A.C. Pereira, P.M. Matias, Nickel–iron–selenium hydrogenases – an overview, Eur. J. Inorg. Chem. 7 (2011) 948–962.
[5] M.J. Pushie, G.N. George, Spectroscopic studies of molybdenum and tungsten enzymes, Coord. Chem. Rev. 225 (2011) 1055–1084.
[6] R.E. Danielle, D.E. Salt, Plants, selenium and human health, Curr. Opin. Plant Biol. 6 (2003) 273–279.
[7] E.A.H. Pilon-Smits, C.F. Quinn, Selenium metabolism in plants, Plant Cell Monographs, 17 2010, pp. 225–241.
[8] A.F. El Mehdawi, E.A.H. Pilon-Smits, Ecological aspects of plant selenium hyperaccumulation, Plant Biol. 14 (2012) 1–10.
[9] J.E. Spallholz, On the nature of selenium toxicity and carcinostatic activity, Free Radic. Biol. Med. 17 (1994) 45–64.
[10] H. Hartikainen, Biogeochemistry of selenium and its impact on food chain quality and human health, J. Trace Elem. Med. Biol. 18 (2005) 309–318.
[11] S. Li, T. Xiao, B. Zheng, Medical geology of arsenic, selenium and thallium in China, Sci. Total Environ. 31 (2012) 31–40.
[12] F. Fordyce, Selenium deficiency and toxicity in the environment, in: O. Selinus, B.J. Alloway, J.A. Centeno, R.B. Finkelman, R. Fuge, U. Lindh, P. Smedley (Eds.), Essentials of Medical Geology Impacts of the Natural Environment on Public Health, Elsevier Academic Press, 2005, pp. 373–415.
[13] S.J. Li, W. Li, X. Hu, L.S. Yang, X. Ruodeng, Soil selenium concentration and Kashin–Beck disease prevalence in Tibet, China, Environ. Sci. Eng. China 3 (2009) 62–68.
[14] L.L. Kang, P. Xu, S.Z. Zhaxi, Z.M. Bashang, X.Y. Li, X. Guo, The changes of hyalurona, nitric oxide and selenium contents in serum for patients with Kashin–Beck disease in Tibet, Chin. J. Endemiol. 25 (2006) 694–696.
[15] M.P. Rayman, S. Stranges, Epidemiology of selenium and type 2 diabetes: can we make sense of it? Free Radic. Biol. Med. 65 (2013) 1557–1564.
[16] A. Griffin, Role of selenium in the chemoprevention of cancer, Adv. Cancer Res. 29 (1979) 419–442.
[17] A. Duffield-Lillico, M. Reid, B. Turnbull, G. Combs Jr., E. Slate, L. Fischbach, J. Marshall, L. Clark, Baseline characteristics and the effect of selenium supplementation on cancer incidence in a randomized clinical trial: A summary report of the nutritional prevention of cancer trial, Cancer Epidemiol. Biomark. Prev. 11 (2002) 630–639.
[18] D. Hatfield, V. Gladyshev, The outcome of selenium and vitamin E cancer prevention trial (SELECT) reveals the need for better understanding of selenium biology, Mol. Interv. 9 (2009) 18–20.
[19] M. Vinceti, C.M. Crespi, C. Malagoli, C. Del Giovani, V. Krogh, Friend or foe? The current epidemiological evidence on selenium and human cancer risk, J. Environ. Sci. Health C Environ. Carcinog. Ecotoxicol. Rev. 31 (2013) 305–341.
[20] S. Stranges, J.R. Marshall, R. Natarajan, R.P. Donahue, M. Trevisan, G.F. Combs, F.P. Cappuccio, A. Ceriello, M.E. Reid, Effects of long-term selenium supplementation on the incidence of type 2 diabetes, Ann. Intern. Med. 147 (2007) 217–223.
[21] D.L. Hatfield, V.N. Gladyshev, The outcome of selenium and vitamin E cancer prevention trial (SELECT) reveals the need for better understanding of selenium biology, Mol. Interv. 9 (2009) 18–20.
[22] E. Humann-Ziehank, Selenium, copper and iron in veterinary medicine – from clinical implications to scientific models, J. Trace Elem. Med. Biol. 37 (2016) 96–103.
[23] F. Garousi, The essentiality of selenium for humans, animals, and plants, and the role of selenium in plant metabolism and physiology, Acta Univ. Sapientiae, Alimentaria 10 (2017) 75–90.
[24] J. Gailer, G.N. George, I.J. Pickering, R.C. Prince, S.C. Ringwald, J.C. Pemberton, R.S. Glass, H.S. Younis, D.W. DeYoung, H.V. Aposian, A metabolic link between As (III) and Se(IV): the seleno-*bis*(S-glutathionyl)arsinium ion, J. Am. Chem. Soc. 122 (2000) 4637–4639.
[25] J.E. Spallholz, L.M. Boylan, M.M. Rhaman, Environmental hypothesis: is poor dietary selenium intake an underlying factor for arsenicosis and cancer in Bangladesh and West Bengal, India? Sci. Total Environ. 323 (2004) 21–32.
[26] G.N. George, J. Gailer, O. Ponomarenko, P.F. La Porte, K. Strait, M. Alauddin, H. Ahsan, S. Ahmed, J.E. Spallhloz, I.J. Pickering, Observation of the seleno *bis*-(S-glutathionyl) arsinium anion in rat bile, J. Inorg. Biochem. 158 (2016) 24–29.
[27] O. Ponomarenko, P.F. La Porte, S.P. Singh, G. Langan, D.E.B. Flemming, J.E. Spallholz, M. Alauddin, H. Ahsan, S. Ahmed, J. Gailer, G.N. George, I.J. Pickering, Selenium-mediated arsenic excretion in mammals: a synchrotron-based study of whole-body distribution and tissue-specific chemistry, Metallomics 9 (2017) 1585–1595.
[28] I.J. Pickering, G.N. George, V. van Fleet-Stalder, T.G. Chasteen, R.C. Prince, X-ray absorption spectroscopy of selenium-containing amino acids, J. Biol. Inorg. Chem. 4 (1999) 791–794.
[29] G.N. George, S.P. Singh, R.C. Prince, I.J. Pickering, The chemical forms of mercury and selenium in fish following digestion with simulated gastric fluid, Chem. Res. Toxicol. 21 (2008) 2106–2110.
[30] M. Korbas, J.L. O'Donoghue, G.E. Watson, I.J. Pickering, S.P. Singh, G.J. Myers, T.W. Clarkson, G.N. George, The chemical nature of mercury in human brain following poisoning or environmental exposure, ACS Chem. Neurosci. 1 (2010) 810–818.
[31] J.J.H. Cotelesage, M.J. Pushie, P. Grochulski, I.J. Pickering, G.N. George, Metalloprotein active site structure determination: synergy between X-ray absorption spectroscopy and X-ray crystallography, J. Inorg. Biochem. 115 (2012) 127–137.
[32] M.J. Pushie, L. Zhang, I.J. Pickering, G.N. George, The fictile coordination chemistry of cuprous-thiolate sites in copper chaparones, Biochim. Biophys. Acta 1817 (2012) 938–947.
[33] J.J. Rehr, R.C. Albers, Theoretical approaches to X-ray absorption fine structure, Rev. Mod. Phys. 72 (2000) 621–654.
[34] L. Zhang, I.J. Pickering, D.R. Winge, G.N. George, X-ray absorption spectroscopy of cuprous-thiolate clusters in *Saccharomyces cerevisiae* metallothionein, Chem. Biodivers. 5 (2008) 2042–2049.
[35] K.B. Musgrave, H.C. Angove, B.K. Burgess, B. Hedman, K.O. Hodgson, All-ferrous titanium(III) citrate reduced Fe protein of nitrogenase: an XAS study of electronic and metrical structure, J. Am. Chem. Soc. 120 (1998) 5325–5326.
[36] H.H. Harris, G.N. George, K.V. Rajagopalan, High resolution EXAFS of the active site of sulfite oxidase: comparison with density functional and X-ray crystallographic results, Inorg. Chem. 45 (2006) 493–495.
[37] G.N. George, X-ray absorption spectroscopy of molybdenum and tungsten enzymes, in: M.L. Kirk, R. Hille, C. Schulzke (Eds.), Molybdenum and Tungsten Enzymes: Spectroscopic and Theoretical Investigations, Royal Society of Chemistry, Series on Metallobiology, 2016, pp. 121–167 (ISBN 978-1-78262-878-1).
[38] S.P. Cramer, O. Tench, M. Yocum, G.N. George, A 13-element Ge detector for fluorescence EXAFS, Nucl. Inst. Methods Phys. Res. A 266 (1988) 586–591.
[39] M.J. Pushie, I.J. Pickering, M. Korbas, M.J. Hackett, G.N. George, Elemental and chemically specific X-ray fluorescence imaging of biological systems, Chem. Rev. 114 (2014) 8499–8541.
[40] S. Vogt, MAPS: a set of software tools for analysis and visualization of 3D X-ray fluorescence data sets, J. Phys. IV France 104 (2003) 635–638.
[41] V.A. Solé, E. Papillon, M. Cotte, P. Walter, J. Susini, A multiplatform code for the analysis of energy-dispersive X-ray fluorescence spectra, Spectrochim. Acta B At. Spectrosc. 62 (2007) 63–68.
[42] L. Li, H. Yan, W. Xu, D. Yu, A. Heroux, W.-k. Lee, S.I. Campbell, Y.S. Chu, B. Lai, A. Somogyi (Eds.), PyXRF: python-based X-ray fluorescence analysis package, Proc. of SPIE, 2017.

[43] C.G. Ryan, D.N. Jamieson, C.L. Churms, J.V. Pilcher, A new method for on-line true-elemental imaging using PIXE and the proton microprobe, Nucl. Inst. Methods Phys. Res. B 104 (1995) 157–165.
[44] C.G. Ryan, D.N. Jamieson, Dynamic analysis: on-line quantitative PIXE microanalysis and its use in overlap-resolved elemental mapping, Nucl. Inst. Methods Phys. Res. B 77 (1993) 203–214.
[45] K. Janssens, B. Vekemans, F. Adams, P. van Espen, P. Mutsaers, Accurate evaluation of μ-PIXE and μ-XRF spectral data through iterative least squares fitting, Nucl. Inst. Methods Phys. Res. B 109–110 (1996) 179–185.
[46] A.M. Crawford, Methodologies in XRF cytometry, Chemistry, University of Michigan, 2015, p. 191 (PhD Thesis).
[47] S.M. Webb, The microanalysis toolkit: X-ray fluorescence image processing software, The 10th International Conference on X-ray Microscopy, AIP Publishing, 2011, pp. 196–199.
[48] A.M. Crawford, N.J. Sylvain, H. Hou, M.J. Hackett, M.J. Pushie, I.J. Pickering, G.N. George, M.E. Kelly, A comparison of parametric and integrative approaches for X-ray fluorescence analysis applied to a stroke model. (unpublished).
[49] J.L. Campbell, J.A. Maxwell, A cautionary note on the use of the Hypermet tailing function in X-ray spectrometry with Si(Li) detectors, Nucl. Inst. Methods Phys. Res. B 129 (1997) 297–299.
[50] R.E. Van Grieken, A.A. Markowicz, Handbook of X-ray Spectrometry, 2 ed., CRC Press, Taylor & Francis, Abingdon, UK, 2002.
[51] L.T. Yi, Z.G. Liu, K. Wang, M. Chen, S.Q. Peng, W.G. Zhao, J.L. He, G.C. Zhao, A new background subtraction method for energy dispersive X-ray fluorescence spectra using a cubic spline interpolation, Nucl. Inst. Methods Phys. Res. A 775 (2015) 12–14.
[52] L.Q. Ren, D. Wu, Y.H. Li, W.R. Chen, H. Liu, Background estimation methods for quantitative X-ray fluorescence analysis of gold nanoparticles in biomedical applications, Biophotonics and Immune Responses Ix, 8944 2014.
[53] C.G. Ryan, E. Clayton, W.L. Griffin, S.H. Sie, D.R. Cousens, SNIP, a statistics-sensitive background treatment, Nucl. Inst. Methods Phys. Res. B (1988) 396–402.
[54] I.J. Pickering, R.C. Prince, D.E. Salt, G.N. George, Quantitative chemically-specific imaging of selenium transformation in plants, Proc. Natl. Acad. Sci. U. S. A. 97 (2000) 10717–10722.
[55] I.J. Pickering, G. Hirsch, R.C. Prince, E.Y. Sneeden, D.E. Salt, G.N. George, Imaging of selenium in plants using tapered metal monocapillary optics, J. Synchrotron Radiat. 10 (2003) 289–290.
[56] S.I. Yang, G.N. George, J. Lawrence, S. Kaminskyj, J. Dynes, B. Lai, I.J. Pickering, Multispecies biofilms transform selenium oxyanions into elemental selenium particles: studies using combined synchrotron X-ray fluorescence imaging and scanning transmission X-ray microscopy, Environ. Sci. Technol. 50 (2016) 10343–10350.
[57] N. Dolgova, M. Hackett, T.C. MacDonald, S. Nehzati, A. James, P. Krone, G.N. George, I.J. Pickering, Distribution of selenium in zebrafish larvae after exposure to organic and inorganic selenium forms, Metallomics 8 (2016) 305–312.
[58] M. Ceko, K. Hummitzsch, N. Hatzirodos, W. Bonner, J. Aitken, D. Russel, M. Lane, R. Rodgers, H. Harris, X-ray fluorescence imaging and other analyses identify selenium and GPX1 as important in female reproductive function, Metallomics 7 (2015) 71–82.
[59] M. Ceko, S. O'Leary, H. Harris, K. Hummitzsch, R. Rodgers, Trace elements in ovaries: measurement and physiology, Biol. Reprod. 94 (2016) 1–14.
[60] C. Weekley, A. Shanu, J. Aitken, S. Vogt, P. Witting, H. Harris, XAS and XFM studies of selenium and copper speciation and distribution in the kidneys of selenite-supplemented rats, Metallomics 6 (2014) 1602.
[61] K.L. Summers, N. Fimognari, A. Hollings, M. Kiernan, V. Lam, R.J. Tidy, D. Paterson, M.J. Tobin, R. Takechi, G.N. George, I.J. Pickering, J.C. Mamo, H.H. Harris, M.J. Hackett, A multimodal spectroscopic imaging method to characterize the metal and macromolecular content of proteinaceous aggregates ("amyloid plaques"), Biochemistry 56 (2017) 4107–4116.
[62] C. Rangacharyulu, C. Roh, Isotopes for combined PET/SPECT imaging, J. Radioanal. Nucl. Chem. 305 (2015) 87–92.
[63] X. Ding, N. Gao, G. Havrilla, Monolithic polycapillary X-ray optics engineered to meet a wide range of applications, Proc. SPIE 4144 (2000) 174.
[64] A.R. Woll, D. Agyeman-Budu, D.H. Bilderback, D. Dale, 3D X-ray fluorescence microscopy with 1.7 μm resolution using lithographically fabricated micro-channel arrays, SPIE Opt. Photonics, 8502 2012 (85020K–1–85020K–14).
[65] A.R. Woll, D. Agyeman-Budu, S. Choudhury, I. Coulthard, A.C. Finnefrock, R. Gordon, E. Hallin, J. Mass, Lithographically-fabricated channel arrays for confocal X-ray fluorescence microscopy and XAFS, J. Phys. Conf. Ser. 493 (1–4) (2014) 012028.
[66] D.N. Agyeman-Budu, S. Choudhury, I. Coulthard, R. Gordon, E. Hallin, A.R. Woll, Germanium collimating micro-channel arrays for high resolution, high energy confocal X-ray fluorescence microscopy, AIP Conf. Proc. 1764 (2016) 020004–0200011.
[67] S. Choudhury, J. Hormes, D.N. Agyeman-Budu, A.R. Woll, G.N. George, I. Coulthard, I.J. Pickering, Application of a spoked channel array to confocal X-ray fluorescence imaging and X-ray absorption spectroscopy of medieval stained glass, J. Anal. At. Spectrom. 30 (2015) 759–766.
[68] B. Kanngießer, W. Malzer, I. Mantouvalou, D. Sokaras, A.G. Karydas, A deep view in cultural heritage—confocal micro X-ray spectroscopy for depth resolved elemental analysis, Appl. Phys. A Mater. Sci. Process. 106 (2012) 325–338.
[69] S. Choudhury, T. Swanston, T. Varney, D.M.L. Cooper, G.N. George, I.J. Pickering, G. Vaughan, B. Bewer, I. Coulthard, Confocal X-ray fluorescence imaging facilitates high resolution elemental mapping in fragile archaeological bone, Archaeometry 58 (2016) 207–217.
[70] S. Choudhury, J.K. Thomas, N.J. Sylvain, O. Ponomarenko, R.A. Gordon, S.M. Heald, D.M. Janz, P.H. Krone, I. Coulthard, G.N. George, I.J. Pickering, Selenium preferentially accumulates in the eye lens following embryonic exposure: a confocal X-ray fluorescence imaging study, Environ. Sci. Technol. 49 (2015) 2255–2261.
[71] B. De Samber, G. Silversmit, K. De Schamphelaere, R. Evens, T. Schoonjans, B. Vekemans, C. Janssen, B. Masschaele, L. Van Hoorebeke, I. Szalóki, F. Vanhaecke, K. Rickers, G. Falkenberg, L. Vincze, Element-to-tissue correlation in biological samples determined by three-dimensional X-ray imaging methods, J. Anal. At. Spectrom. 25 (2010) 544–553.
[72] G. Silversmit, B. Vekemans, S. Nikitenko, S. Schmitz, T. Schoonjans, F.E. Brenker, L. Vincze, Spatially resolved 3D micro-XANES by a confocal detection scheme, Phys. Chem. Chem. Phys. 12 (2010) 5653–5659.
[73] P. Glatzel, U. Bergmann, High resolution 1s core hole X-ray spectroscopy in 3d transition metal complexes – electronic and structural information, Coord. Chem. Rev. 249 (2005) 65–95.
[74] D. Sokaras, T.-C. Weng, D. Nordlund, R. Alonso-Mori, P. Velikov, D. Wenger, A. Garachtchenko, M. George, V. Borzenets, B. Johnson, T. Rabedeau, U. Bergmann, A seven-crystal Johann-type hard X-ray spectrometer at the Stanford Synchrotron Radiation Lightsource, Rev. Sci. Instrum. 84 (2013) 053102.